

***Operando* Electrochemical Kinetics in Particulate Porous Electrodes by Quantifying the Mesoscale Spatiotemporal Heterogeneities**

Shubham Agrawal¹ and Peng Bai^{1,2,*}

¹Department of Energy, Environmental & Chemical Engineering, Washington University in St. Louis, St. Louis, Missouri – 63130, United States

²Institute of Materials Science and Engineering, Washington University in St. Louis, St. Louis, Missouri – 63130, United States

*Email: pbai@wustl.edu

Abstract

Electrochemical energy systems rely on particulate porous electrodes to store or convert energies. While the three-dimensional porous structures were introduced to maximize the interfacial area for better overall performance of the system, spatiotemporal heterogeneities arose from materials thermodynamics localize the charge transfer processes onto a limited portion of the available interfaces. Here, we demonstrate a simple but precision method that can directly track and analyze the *operando* (i.e. local and reacting) interfaces at the mesoscale in a practical graphite porous electrode to obtain the true local current density, which turned out to be two orders of magnitude higher than the globally averaged current density adopted by existing studies. Our results resolve the long-standing discrepancies between kinetics parameters derived from electroanalytical measurements and from first principles predictions. Contradictory to prevailing beliefs, the electrochemical dynamics is not controlled by the solid-state diffusion process once the spatiotemporal reaction heterogeneities emerge in porous electrodes.

Electrochemical energy storage and conversion systems are critical for a sustainable future¹. Lithium-ion batteries (LIBs) that offer the highest energy density have revolutionized electronic devices, portable power tools and electric cars²⁻⁴. But their further advancements have been impaired by the random occurrences of elusive safety accidents^{5,6}, which are believed to originate from microscopic heterogeneities in the particulate porous electrodes⁷. State-of-charge (SOC) heterogeneities have recently been identified in both the solid-solution⁸⁻¹² and phase-transforming electrodes¹³⁻¹⁹, as a direct result of non-uniform distribution of electrochemical reactions due to either the structures of the composite porous electrodes^{8,20} or the thermodynamics of the active materials^{21,22}. While the nanoscale heterogeneities in individual particles detected by synchrotron X-ray provide deep insights on the possible degradation mechanisms, the evolutions of the heterogeneities among hundreds of particles sitting in realistic surroundings are critical for the understanding of the true local electrochemical kinetics that dictate the real-time performance.

The immediate consequence of the spatiotemporal heterogeneities is that the actual reacting interfacial area at any instant, i.e. area of the *operando* interfacial area, is only a small portion of the total available interfacial area usually obtained from the Brunauer-Emmett-Teller (BET) method. Given that existing electroanalytical techniques^{23,24} rely on the square-law scaling $D_{Li^+} \sim [I(t)/S]^2$ to extract the diffusion coefficient D_{Li^+} from the total current $I(t)$ and the assumed *constant total* interfacial area S , the electrochemical kinetics in systems with strong heterogeneities may have been misinterpreted due to the smaller *operando* interfacial area. As one of the most widely used electrodes for both the nonaqueous^{15,25} and aqueous²⁶ batteries, graphite electrodes²⁷ are known to have strong reaction heterogeneities^{13,15} reflected by its particle-by-particle reaction mechanism^{15,21}. Depending on the choices of interfacial area, the lithium-ion diffusion coefficient in graphite (D_{Li^+}) extracted by the traditional electroanalytical methods varies by about 8 orders of magnitude in the literature²⁸⁻³⁶. Still, D_{Li^+} obtained during phase transformation were always about 2 orders of magnitude lower than the average^{29,35}. The discrepancy has long been doubted as the inaccuracy of the interfacial area³⁷, but direct experimental evidence is still missing. Similar orders-of-magnitude discrepancies also exist in other porous electrodes composed of phase-transforming²⁴ or solid-

solution particles³⁸⁻⁴⁰, missing satisfactory explanations. The discrepancies in the kinetic parameters directly affect the determination of the rate-limiting step, and thereafter undermine the validity of traditional electroanalytical techniques and the effectiveness of the predicted rational design guidance.

Here, we use graphite as our model system to demonstrate the direct quantification of the true local current densities for precision electrochemical kinetics. The unique color changing property during graphite lithiation^{15,36} allows us to develop economical *operando* platform with optical microscope to investigate the dynamics of the heterogeneities at high speed and at the mesoscale (imaging hundreds of particles simultaneously every two seconds). Our study reveals that the state of charge (SOC) heterogeneities are indeed the result of reaction heterogeneities, which lead to the localization of reaction flux onto a limited number of particles in the electrode. Using the moving phase boundaries between different stages (phases) to approximate the *operando* electrochemical interfacial area, the true local current density was determined to be about 2 orders of magnitude higher than the globally averaged current density. Without presumptions on the rate-limiting steps, our further analyses suggest that, once the heterogeneities emerge, the *operando* (i.e. local and working) electrochemical kinetics of the porous electrode is not diffusion-limited. The diffusion coefficients obtained using our new method resolve the long-standing huge discrepancies between experiments and theoretical predictions.

Spatiotemporal heterogeneities.

Figure 1 demonstrates the color evolution in a thin graphite electrode during a potentiostatic intermittent titration technique (PITT) experiment from 275 mV to 0.1 mV (vs. Li/Li⁺), with a step size of 10 mV and threshold current of C/20. The entire lithiation process can be divided into three segments. Segment (I) is before the voltage stepping from 85 mV to 75 mV shown in Fig. 1. During the voltage hold at 75 mV, Segments (II) and (III) were identified and divided by phase transformation features.

In segment (I) all empty particles (dark grey) reacted concurrently regardless of their morphology and size, until they all turned blue (Stage 3). At this point, the blue particles accommodated 23% of the total capacity supplied in the entire PITT discharge and brought down the cell voltage from 275 mV to 85 mV. Since, at this moment ($t = 0$ s shown in Fig. 1), all the particles were in Stage 3 (blue), the SOC associated

with Stage 3 was determined to be the global SOC of the electrode, i.e. $x_B = 23\%$, slightly higher than the values adopted in earlier works^{15,41}.

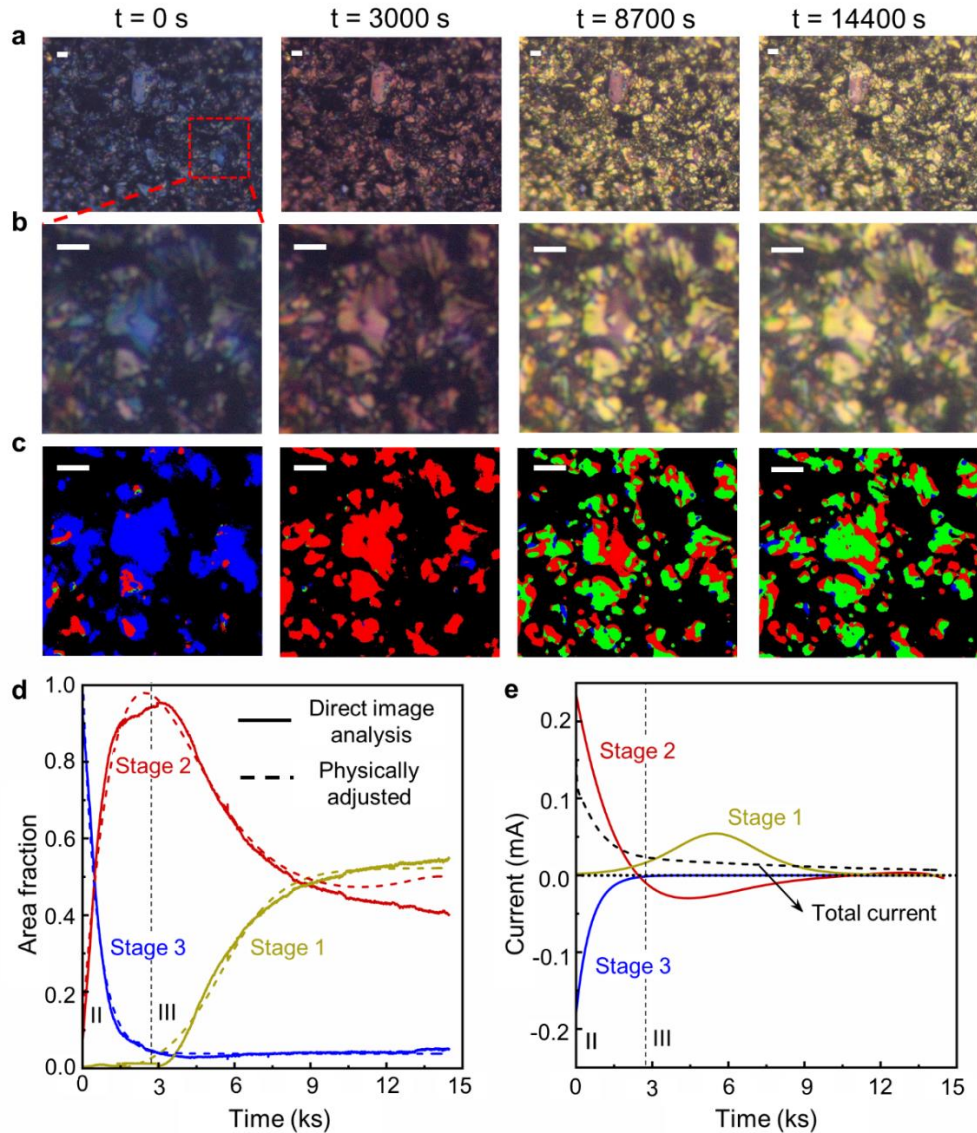


Figure 1: Evolution of stages during Li^+ ion intercalation during the voltage stepping from 85 mV to 75 mV vs Li/Li^+ . **a**, Snapshots of the entire viewing area under the optical microscope with the 50x objective, at four times: $t = 0$ s, 3000 s, 8700 s and 14400 s. **b**, Magnified photos highlighting the coexistence of different stages intra- and inter- particles. **c**, The converted RGB images showing the actual area fraction quantified by ImageJ. The observed blue, red and gold colors were converted to standard blue, red and green colors, respectively. **d**, The evolution curves of the colored areas during the voltage stepping, obtained from the direct image analysis along with the physically adjusted analytical curves (refer Supplementary Information Section 8 for details). **e**, The derived phase currents based on the time-derivative of the physically adjusted area evolution curves. **Scale bar: $5 \mu\text{m}$**

In segment (II), a few blue particles began to turn red at the onset of the PITT voltage stepping from 85 mV to 75 mV. The localized red (Stage 2) region always coexisted with the blue (Stage 3) regions within the same particle. The evolving boundaries between the red and blue regions clearly reveal the phase transformation process. Upon careful visual inspection, we observed that the Li^+ ion flux prefers to go into particles with phase boundaries. The remaining blue (Stage 3) particles will begin receiving Li^+ ion flux only after existing boundary-containing phase-transforming particles become completely red. The red particles then remain inactive, waiting for all the other particles to reach the same stage. This process is consistent with the particle-by-particle reaction mechanism of LiFePO_4 electrodes at low current densities²¹. Similarly, we determine the SOC associated with Stage 2 (x_R) to be 55%, which is the global SOC when all particles turned red. In segment (III), while the cell is still under the voltage held at 75 mV, the red particles start a similar particle-by-particle phase transformation process to turn gold (Stage 1). The SOC associated with Stage 1 (x_G) is calibrated 100% based on equilibrium experiments (Supplementary Fig. 5). By converting the color into standard RGB map (Fig. 1c), we were able to exclude the all-time inactive regions and accurately quantify the areas covered by the three colors (Stages) in nearly 15,000 *operando* images. The sequential reaction process is quantitatively reflected by the evolution curves of the area fractions for different colors, shown in Fig. 1d.

Currents carried by individual colors (phases)

With the SOCs for each color determined above, i.e. $x_B = 23\%$, $x_R = 55\%$, $x_G = 100\%$, the area fraction evolution curves can be converted into capacity evolution curves (Supplementary Fig. S8), by $Q_i = x_i a_i(t) q_o A_T$. Here, i represents Blue, Red, and Gold colors. Q_i and a_i are the capacity and the area fraction of color i . q_o is the areal capacity of the entire electrode, and A_T is the total area of particles accounted in the image analysis. The capacity curves directly converted from experimental data were physically adjusted based on charge conservation, to exclude possible system and sampling errors. By further taking the first-order time-derivative of the charge associated with each color, the phase current can be obtained via,

$$I_i(t) = \frac{dQ_i}{dt} = x_i q_o A_T \left(\frac{da_i}{dt} \right) \quad (1)$$

Figure 1d of the derived phase currents suggest that the stable phases/stages grow or diminish faster than the rate of charge supply (total current), which points towards the direction that the rate enabled the phase boundary propagation is much higher than the reaction rate estimated by using the total current. Since Li^+ ions insert into graphite through the edge planes, not through the basal plane that reveal the colors, the area of the phase boundary, i.e. length of the phase boundary times the thickness of the particle, must be determined, in order to obtain the true local current density.

***Operando* interfacial current densities.**

In principle, Li^+ ions can intercalate into graphite particles from anywhere on the edge planes to form a shrinking-core type pattern, as observed in a 50- μm graphite disk⁴² and 400- μm graphite flake⁴³. For our graphite particles with a mean particle size of 8.13 μm (Supplementary Fig. S3), however, ion intercalations appear to occur only on a limited portion of the particle perimeter. The phase boundary, originated from the edge, quickly straightens itself to form an intercalation wave to propagate through the remaining body of the particle (Fig. 2a). Since we only observed color change at the phase boundaries and not in the stable regions during Li^+ ion intercalation, the net flux within any color is conserved, and that led to the movement of phase boundary is identical to the reaction flux at the particle edges. Based on this observation, we propose to use the mathematical product of the total length of the phase boundaries and the thickness of the graphite particles as the true *operando* interfacial area within the porous electrodes. With proper Boolean operations (see Methods and Supplementary Fig. S5), the length of the phase boundaries can be determined by ImageJ. As shown in Fig. 2b, the total length of the Blue-Red (L_{BR}) boundaries increased at the beginning of the voltage stepping from 85 mV to 75 mV, then decreased toward zero in a time span of 2900 s. While the total length of the Red-Gold boundaries (L_{RG}) slightly increased at the onset of voltage stepping, it remained relatively constant at a value close to zero. The trend is consistent with the decaying of the global total current. At the moment L_{BR} decayed to nearly zero and stopped changing, a rapid increase in L_{RG} was observed, corresponding to the onset of phase transformation from Red (Stage 2) to Gold (Stage 1), while the global total current was still decreasing, indicating a dramatic change of the actual interfacial

current density. L_{RG} maintained a steady growth and became almost constant as the global current began to saturate.

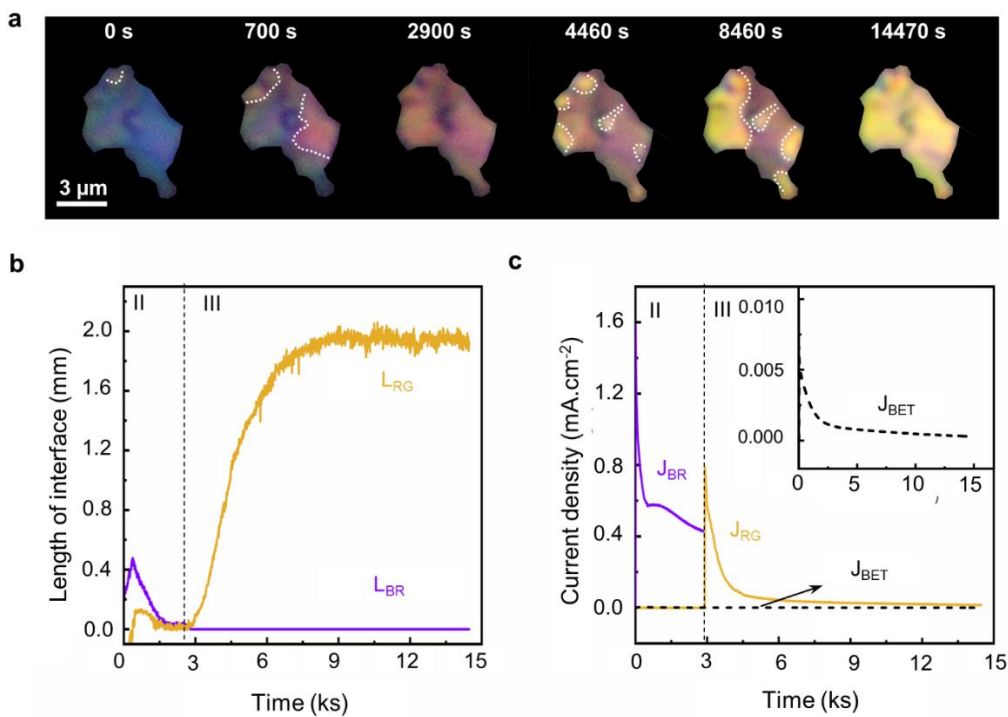


Figure 2: Evolution of the total lengths of phase boundaries and the associated local current densities. **a**, Moving phase boundaries (white dotted lines) within a typical graphite particle during the 85 mV – 75 mV voltage stepping. **b**, Evolutions of the total lengths of interfaces between blue and red regions and between red and gold regions during the voltage step, determined from the direct image analysis of the viewing area of the electrode. **c**, The current density calculated based on the effective *operando* interfacial area. Inset shows the globally average current density based on the BET surface area.

By multiplying the total length of the phase boundaries determined from direct image analysis with the thickness of our graphite particles (see Methods), the *operando* interfacial area and therefore the *operando* interfacial current density, i.e., the truly working local current density, can be estimated. As shown in Fig. 2c, the *operando* interfacial current densities are about two orders of magnitude higher than the globally averaged current density based on the BET area (9.424 m²/g). This two-orders-of-magnitude discrepancy will be amplified to a four-orders-of-magnitude difference in the derived diffusion coefficients, via the

square-law scaling of the traditional electroanalytical methods^{23,24}. This discrepancy questions the prevailing belief that the rate-limiting step of Li⁺ ion intercalation in graphite is the bulk diffusion.

Kinetic parameters from reaction-limited and mix-controlled processes.

The *operando* interfacial current densities determined above can be plotted against $1/\sqrt{t}$ to perform a kinetic analysis⁴⁴. The lack of a straight line (predicted by the classic Cottrell equation) suggests that the process is likely not diffusion-limited. Instead, using the modified PITT model^{45,46} (mPITT) without presumption of the rate-limiting step, the dynamic process can be investigated more rigorously in two dynamic regimes,

$$J(t) = \frac{D_{Li^+}Q}{lV_T} B \exp\left(B^2 \frac{D_{Li^+}t}{l^2}\right) \operatorname{erfc}\left(B \sqrt{\frac{D_{Li^+}t}{l^2}}\right), \quad t \ll \frac{l^2}{D_{Li^+}} \quad (2a)$$

$$\ln[J(t)] = -\lambda_1^2 \left(\frac{D_{Li^+}t}{l^2}\right) + \ln\left[\frac{2QD_{Li^+}}{lV_T} \frac{B^2}{(\lambda_1^2 + B^2 + B)}\right], \quad t \gg \frac{l^2}{D_{Li^+}} \quad (2b)$$

where $J(t)$ is the transient local current density, B is the electrochemical Biot number, t the step time, l the diffusion length, set to be one half of the dimension of basal plane²⁹, i.e. 4 μ m for our case. erfc represents the complementary error function. λ_1 is the first order positive root of equation⁴⁵ $\lambda_1 \tan \lambda_1 = B$. Q is the total capacity transferred during the respective time. V_T is the total volume of the particles in the electrode.

With the *operando* interfacial current densities identified in Fig. 2c, Eq (2a) was used to fit the diffusion coefficient D_{Li^+} and the electrochemical Biot number, by minimizing the least squares (Figs. 3a-3c). Among all the recorded phase transformations, only the Red to Gold transformation was long enough to enter in the regime of $t \gg l^2/D_{Li^+}$, which was fitted by Eq. (2b) for $t > 4000$ s (Supplementary Fig. 9). A critical feature of the mPITT model⁴⁵ is that the apparent two independent fitting parameters are actually constrained by the system-specific exchange current density (j_0) via the definition of Biot number, $B = -j_0 l (\partial U / \partial C) / (D_{Li^+} RT)$. Here, $\partial U / \partial C$ is the derivative of the open-circuit voltage (OCV) with respect to the solid-state Li⁺ ion concentration, as explained in the Supplementary Information (Section 11). R is the gas constant and T is the temperature. While the mPITT method itself allows the evaluation of j_0 ,

independent electrochemical impedance spectroscopy (EIS) experiments were performed on the same *operando* cell to obtain physical justification and validation for the curve fittings. By analyzing the Nyquist plots with the equivalent circuit model (Supplementary Fig. S11), the charge-transfer resistance (R_{CT}) can be obtained to calculate the exchange current density via⁴⁶ $j_0 = RT/(FA R_{CT})$. Here, A is the *operando* interfacial area, and F is the Faraday constant. Using the room temperature of $T = 298\text{K}$, a good agreement was found between the exchange current densities obtained from EIS and from mPITT (Fig. 3d).

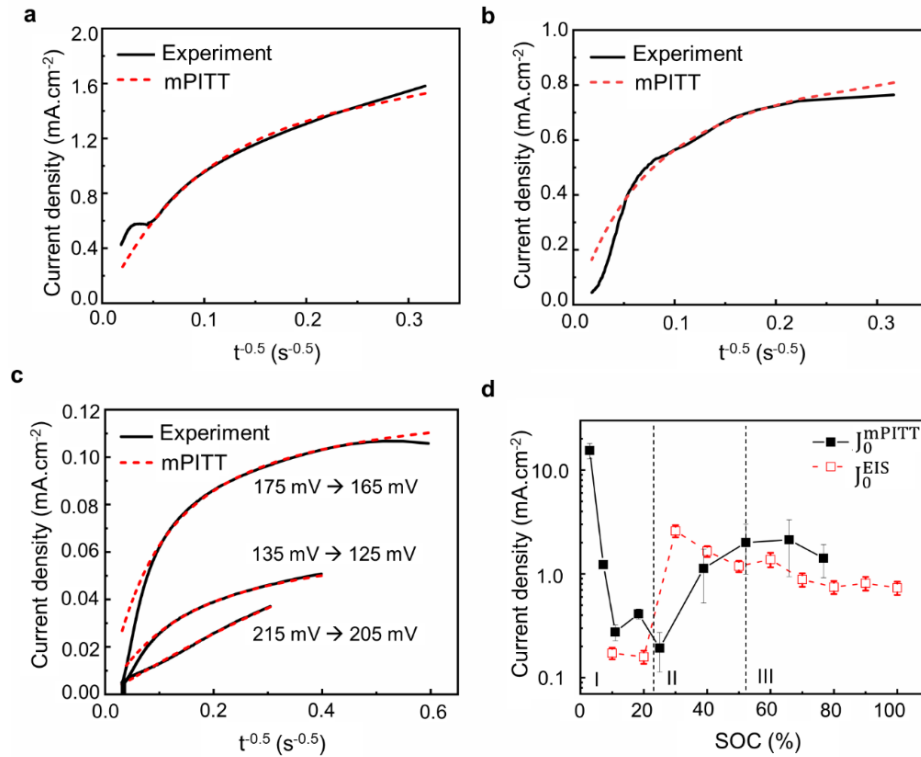


Figure 3: Comparison between the *operando* interfacial current density and the modified PITT model. Fitting results of *operando* interfacial current density during **a**, Blue to Red phase transformation (J_{BR}), **b**, Red to Gold phase transformation (J_{RG}), and **c**, the solid-solution region from 215 mV – 125 mV. **d**, Comparison between exchange current densities extracted from the mPITT model and independent Electrochemical Impedance Spectroscopy (EIS) experiments at various SOC levels.

As shown in Fig. 4, the Li^+ ion diffusion coefficients into graphite (black solid line) fitted from the mPITT model using the *operando* interfacial area determined from direct image analysis lie in a relatively narrow range of $6.39 \times 10^{-11} - 4.71 \times 10^{-10} \text{ cm}^2 \text{ s}^{-1}$. Owing to the *operando* interfacial area, the

diffusion coefficients in the SOC range with phase transformations no longer drop by two orders of magnitude, as reported in earlier studies^{29,35}. The electrochemical Biot number (red dashed line) decreases during lithiation into graphite, indicating the transition from diffusion-limited process to the mix-controlled, and finally to the reaction-limited process, marked by vertical dashed lines in Fig. 4. Although the occurrences of major voltage steps ($t > 500s$) during the entire PITT experiment vary in five different *operando* cells, the fundamental mechanism of the Li^+ ion intercalation follows similar trend, yielding Li^+ ion diffusion coefficients and Biot numbers in the same orders of magnitude (Supplementary Fig. 10). As anticipated, the diffusion coefficients identified here are nearly four orders of magnitude higher than that extracted from traditional methods considering a diffusion-limited Cottrell mechanism ($1.18 \times 10^{-14} \text{ cm}^2 \text{ s}^{-1}$), yet using the BET-averaged current density. Our results provide the straightforward evidence that for $\text{SOC} > 9\%$, Li^+ ion diffusion into graphite can be considered a fast process, as speculated by earlier studies^{30,36,45}. Once the spatiotemporal heterogeneities emerge, the process is no longer diffusion-limited, consistent with a recent scaling analysis⁴³.

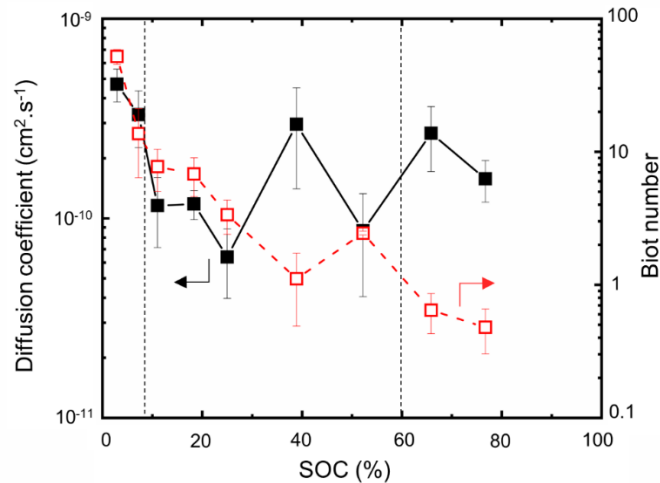


Figure 4: SOC-dependent diffusion coefficients and electrochemical Biot numbers from 5 sets of independent *operando* experiments. Symbols represents the mean value. Error bars indicate the standard deviation. Vertical dashed lines mark $B = 10$ and $B = 1$, which divide the SOC range into diffusion-limited ($\text{SOC} < 9\%$), mix-controlled ($9\% < \text{SOC} < 60\%$), and reaction-limited ($\text{SOC} > 60\%$).

Discussion.

The spatiotemporal heterogeneities observed in porous electrodes made of phase-transforming materials are largely caused by the mesoscale particle-by-particle reaction mechanism^{15,21,47}. Due to the nucleation barrier for the ion intercalation-induced solid-state phase transformation⁴⁸, competition on the intercalation flux could even occur between two identical particles with exactly the same electrochemical surroundings, which means that the heterogeneity will emerge in electrodes with perfectly uniform distributions of active particles, pores (electrolyte), conductive additives and polymer binders. While higher total currents, and therefore higher overpotentials, were found to promote concurrent reactions among many in-plane particles²¹, they unavoidably promote dynamic heterogeneities along the thickness of the porous electrode, i.e. among cross-plane particles¹⁸. Eliminating the dynamic heterogeneities may still be achieved by altering the nucleation behavior. Reducing the particle size has been confirmed an effective approach to remove the nucleation barrier thermodynamically^{49–51}. It is worth mentioning that, contradictory to the prevailing understandings, the purpose of reducing the particle size here is not to mitigate the “slow” solid state diffusion, as we have demonstrated here that the system is not diffusion-limited. Reducing particle sizes will help to bring the system from the mix-controlled regime to purely reaction-limited regime⁴³.

As opposed to the homogeneous reactions in solutions, reactions occurring on the electrode surface were named heterogeneous reactions. However, investigations targeting the spatiotemporal heterogeneities have been limited until recently^{52–54}. The huge difference between the available interfacial area and the *operando* interfacial area raises a fundamental question: whether the electrochemical response from electrodes under small excitations (e.g. low total current) can be considered from quasi- or near-equilibrium behaviors. Our results clearly show that the apparently low total current was actually distributed to about 1% of the available interfacial area, leading to a significantly higher local current density than expected. The electrochemical responses of the electrode (total current and voltage) are therefore collective contributions of far-from-equilibrium behaviors from only a small portion of the electrode. The results remind the necessity and importance to always confirm the consistency between the collective electrochemical responses and the actual contributing parts in the electrode.

Our method is not limited to the PITT technique. Revealing the mesoscale spatiotemporal heterogeneities under other types of electrochemical excitations (e.g. galvanostatic cycling, cyclic voltammetry, etc.) will lead to critical refinements to existing understandings of the electrochemical kinetics and rate-limiting steps. For electrode materials without this unique visible color-changing property, Raman spectroscopy appears to an effective monitoring approach to achieve the heterogeneity map⁵⁵, which can be further analyzed following our methods to obtain the *operando* interfacial kinetics. It is noteworthy that, for graphite electrode made of flake-type particles, using just the traditional electrochemical method with the constant *geometric* area of the electrode yields diffusion coefficients in the similar range (10^{-10} - 10^{-9} cm² s⁻¹). While this coincidence can be utilized as a rule-of-thumb estimation for the *operando* interfacial area, it is difficult to be justified physically by the microscopic dynamics within individual particles, as reflected by the unphysical huge drops of diffusion coefficients whenever phase separation occurs. Incorporating the dynamic *operando* interfacial area into various modified battery models^{15,56-62} that consider the intra- and inter-particle phase transformation physics will enable more effective guidance for the rational design of particulate porous electrodes.

Conclusion.

By exploiting the colorimetric behavior of lithiated graphite, we have demonstrated a direct, simple, yet precision method to monitor and quantify the spatiotemporal heterogeneities in particulate porous electrodes. The true local current density, i.e. the *operando* interfacial current density by our definition, obtained from direct image analysis is ~100 times higher than the BET-average current density. Although all the particles in the porous electrodes are electrochemically active and eventually get fully intercalated with the Li⁺ ions, at any time instant, only a limited number of particles and limited portion of the total available interfacial area receive the ionic flux. Our *operando* monitoring clearly revealed that once a successful nucleation event occurs and phase boundaries start to form in a randomly chosen particle, it is preferred for further intercalation irrespective of its shape and size. Since the Li⁺ intercalation into graphite particles is not diffusion-limited, smaller particles do not necessarily provide a substantial improvement in the high-rate performance. However, reducing particle size may help eliminate the reaction heterogeneities

by altering the nucleation barrier for solid-state phase transformation in individual particles, such that the concurrent reaction pathway become thermodynamically favorable, which is beneficial for the cycle life and safety.

Methods

Thin electrode preparation: Graphite flakes (7-10 μm , 99%, Alfa-Aesar), PVdF binder (>99.5%, MTI Corp) and conductive acetylene black powder (35-40 nm, MTI Corp) were mixed in the ratio 88:10:2 and dissolved in 1-methyl-2-pyrrolidone (NMP, 99.5%, Sigma Aldrich) to form a homogeneous slurry. To ensure the best imaging quality, the slurry was coated onto separator film by the doctor-blade method. The electrodes were dried at 60°C to remove the NMP. $\Phi 8$ mm electrodes were punched out and were kept under vacuum at 70°C for 12 hours to remove the residual moisture. The active material loading, and electrode thickness were 0.7 mg cm^{-2} and 5 μm , respectively. The SEM images of the electrode are shown in the Supplementary Fig. S1.

Operando setup and experiments. A half-cell using the thin graphite electrode, a Li anode, a glass-fiber separator, and 1M LiPF_6 in EC:DMC (50:50 v/v) in a standard 2032 coin cell with a 2 mm hole on the top, was assembled in an Ar-filled glovebox. A 5 x 5 mm glass window was attached using epoxy to seal the cell and view the graphite flakes under the optical microscope. The coin cell was placed on a stage of the Olympus BX53M microscope under objective 50x for *operando* observation. The cell was cycled at C/4 current five times between cut-off voltages 1.5V and 0.4 mV, to form a stable SEI. We then, performed a PITT discharge from 275 mV to 0.1 mV, with 10 mV step size and C/20 threshold current, while capturing the time frames every 10s. All the acquired digital photos were processed using ImageJ to quantify the colored regions. The detailed description of the procedures is mentioned below. See sections 5-7 of the Supplementary Information for more details.

An Electrochemical Impedance Spectroscopy (EIS) was conducted at intervals of 10% SOC from 10% to 100% SOC. The cells were discharged at 0.1C current to the relevant SOC and relaxed for 2h to reach equilibrium before taking the EIS measurements. All the EIS measurements were taken at 10 mV amplitude in the frequency range 1 MHz – 1 Hz. The obtained Nyquist plots (Supplementary Fig. S12-S16) were fitted using the equivalent circuit model, shown in Supplementary Fig. S11.

Color thresholds for area quantification. The built-in Hue-Saturation-Brightness threshold method of ImageJ was used to identify the blue, red and gold colors in the photos captured in the *operando* PITT

experiment. ImageJ auto-selects the brightness to accommodate all the non-black regions/graphite flakes. All the grey/unreacted regions were first selected between the saturation range 0 – 40 and were converted to black. A fixed range of hue was used to select similar colored regions (Red: 0 – 24, Gold: 24 – 44, and Blue: 44 – 255) while maintaining the same range of saturation (40 – 255) and brightness. The leftover regions or the surrounding matrix, calibrated out at 100% SOC, were converted to the standard black color. The above criteria were applied to all the photos with the help of a script.

Charge conservation calibration. The area evolution curve in Fig. 1c was investigated to understand how the stable phases change, which is responsible for the surface reaction, by applying the charge conservation within the electrode, $\sum_i q_i A_i(t) = q_T(t) A_T$, where i represents Blue, Red, and Gold, q_i is the areal capacity of the i^{th} color and can be calculated from the SOC of the i^{th} color (estimated above) and the theoretical areal capacity of the material (q_o), $q_i = x_i q_o$, A_i is the area covered by i^{th} color, q_T is the areal capacity of the electrode and A_T is the total surface area of particles in the electrode. The above equation can, then be transformed into $\sum_i x_i a_i(t) = x_T(t)$ where a_i is the area fraction of the i^{th} color, and x_T is the global SOC of the electrode. For known area fractions of stable phases, a phase-transforming material should inherently follow this equation. Since we only observed a $100 \times 100 \mu\text{m}$ window under the optical microscope, the validity of the above equation for the observed region confirms that the analysis can be confidently extrapolated to the entire electrode (Supplementary Fig. S8).

Curve validation and physical adjustment. The capacity carried by each stage during the PITT discharge was calculated using $Q_i = q_i A_i(t) = x_i q_o a_i(t) A_T$, as explained in the main text. The equation is valid because the intercalation process satisfied the equation $\sum_i x_i a_i(t) = x_T(t)$ during the entire PITT (See Supplementary Information Section 8). The individual capacity contribution follows the same trend as the area fraction evolution curve in Fig. 1c. They were individually represented by analytical expressions, for instance, Stage 3 by an exponential curve, Stage 2 by a 6th order polynomial equation and Stage 1 by a logistic S-shaped curve. A detailed description with fitting parameters is provided in the Supplementary

Information Section 8. The phase currents were calculated by taking a 1st order time derivative of the obtained analytical expressions (Equation 1).

Small noises were observed while estimating the length of interface using ImageJ (Fig. 2a) due to errors arising in the pixel-by-pixel measurement. We removed this noise by applying a quadratic regression method in MATLAB, enabling us to obtain smooth interfacial current densities.

Determination of Interface Area: For a shape with two colors, ImageJ can be used to find the perimeter covered by each color, and the outer perimeter of the shape, which together can be solved for the length of the interface. In our case, particles existed in three different states at a time. To calculate the length of the interface, for instance, the Blue – Red interface, we relied on the fact that the phase transformation in graphite can only occur in one order: Stage 3 to Stage 2 to Stage 1. We converted all the green regions in the transformed RGB images, to the standard red color, thus eliminating all Red – Gold interfaces. This enabled us to find the length of the Blue – Red interface using the above methodology from the following equation, $L_{BR} = \frac{l_{Blue} + l_{Red} - l_{particles}}{2}$. Similarly, we calculated the length of the Red – Gold interface by converting all the blue regions to the standard red and applying following equation, $L_{RG} = \frac{l_{Red} + l_{Gold} - l_{particles}}{2}$ where L_{BR} and L_{RG} are the lengths of Blue – Red and Red – Gold interfaces respectively, l_{Blue} , l_{Red} and l_{Green} are the perimeters of the blue, red and gold regions in the corresponding transformed images, and $l_{particles}$ is the outer perimeter of all the particles within the viewing frame.

Considering disc-shaped flakes with an average diameter 8 μ m and thickness 0.5 μ m, our ~5 μ m thick electrode constituted ~10⁷ particles with 10 layers stacked over each other. On making a statistical assumption that all layers were similar, we calculated the active area by multiplying the total length of interface with the electrode thickness.

References

1. Chu S, Cui Y, Liu N. The path towards sustainable energy. *Nat Mater.* 2016;16(1):16–22.
2. Tarascon JM, Armand M. Issues and challenges facing rechargeable lithium batteries. *Nature.* 2001;414(6861):359–67.
3. Choi JW, Aurbach D. Promise and reality of post-lithium-ion batteries with high energy densities. *Nat Rev Mater.* 2016;1.
4. Goodenough JB, Kim Y. Challenges for rechargeable Li batteries. *Chem Mater.* 2010;22(3):587–603.
5. Williard N, He W, Hendricks C, Pecht M. Lessons learned from the 787 dreamliner issue on Lithium-Ion Battery reliability. *Energies.* 2013;6(9):4682–95.
6. Liu X, Ren D, Hsu H, Feng X, Xu GL, Zhuang M, et al. Thermal Runaway of Lithium-Ion Batteries without Internal Short Circuit. *Joule.* 2018;2(10):2047–64.
7. Harris SJ, Lu P. Effects of inhomogeneities -Nanoscale to mesoscale -on the durability of Li-ion batteries. *J Phys Chem C.* 2013;117(13):6481–92.
8. Tian C, Xu Y, Nordlund D, Lin F, Liu J, Sun Z, et al. Charge Heterogeneity and Surface Chemistry in Polycrystalline Cathode Materials. *Joule.* 2018;2(3):464–77.
9. Gent WE, Li Y, Ahn S, Lim J, Liu Y, Wise AM, et al. Persistent State-of-Charge Heterogeneity in Relaxed, Partially Charged $\text{Li}_{1-x}\text{Ni}_3\text{Co}_3\text{Mn}_3\text{O}_2$ Secondary Particles. *Adv Mater.* 2016;28:6631–8.
10. Nanda J, Remillard J, O'Neill A, Bernardi D, Ro T, Nietering KE, et al. Local state-of-charge mapping of lithium-ion battery electrodes. Vol. 21, *Advanced Functional Materials.* 2011. p. 3282–90.
11. Nakamura T, Watanabe T, Kimura Y, Amezawa K, Nitta K, Tanida H, et al. Visualization of Inhomogeneous Reaction Distribution in the Model LiCoO_2 Composite Electrode of Lithium Ion Batteries. *J Phys Chem C.* 2017;121(4):2118–24.
12. Fang S, Yan M, Hamers RJ. Cell design and image analysis for in situ Raman mapping of

- inhomogeneous state-of-charge profiles in lithium-ion batteries. *J Power Sources*. 2017;352:18–25.
13. Harris SJ, Timmons A, Baker DR, Monroe C. Direct in situ measurements of Li transport in Li-ion battery negative electrodes. *Chem Phys Lett*. 2010;485(4–6):265–74.
 14. Qi Y, Harris SJ. In situ observation of strains during lithiation of a graphite electrode. *J Electrochem Soc*. 2010;157(6):741–7.
 15. Thomas-alyea KE, Jung C, Smith RB, Bazant MZ. In Situ Observation and Mathematical Modeling of Lithium Distribution within Graphite. 2017;164(11):E3063.
 16. Liu J, Kunz M, Chen K, Tamura N, Richardson TJ. Visualization of charge distribution in a lithium battery electrode. *J Phys Chem Lett*. 2010;1(14):2120–3.
 17. Chueh WC, El Gabaly F, Sugar JD, Bartelt NC, McDaniel AH, Fenton KR, et al. Intercalation pathway in many-particle LiFePO₄ electrode revealed by nanoscale state-of-charge mapping. *Nano Lett*. 2013;13(3):866–72.
 18. Liu H, Kazemiabnavi S, Grenier A, Vaughan G, Di Michiel M, Polzin BJ, et al. Quantifying Reaction and Rate Heterogeneity in Battery Electrodes in 3D through Operando X-ray Diffraction Computed Tomography. *ACS Appl Mater Interfaces*. 2019;11(20):18386–94.
 19. Yang Y, Xu R, Zhang K, Lee S-J, Mu L, Liu P, et al. Quantification of Heterogeneous Degradation in Li-Ion Batteries. *Adv Energy Mater*. 2019;9(25):1900674.
 20. Levi MD, Sigalov S, Salitra G, Nayak P, Aurbach D, Daikhin L, et al. Collective phase transition dynamics in microarray composite Li_xFePO₄ electrodes tracked by in situ electrochemical quartz crystal admittance. *J Phys Chem C*. 2013;117(30):15505–14.
 21. Li Y, El Gabaly F, Ferguson TR, Smith RB, Bartelt NC, Sugar JD, et al. Current-induced transition from particle-by-particle to concurrent intercalation in phase-separating battery electrodes. *Nat Mater*. 2014;13(12):1149–56.
 22. Zhang W, Yu HC, Wu L, Liu H, Abdellahi A, Qiu B, et al. Localized concentration reversal of lithium during intercalation into nanoparticles. *Sci Adv*. 2018;4(1):1–12.
 23. Bard AJ, Faulkner LF. *Electrochemical Methods: Fundamentals and Applications*. 2nd ed. 2001.

24. Zhu Y, Gao T, Fan X, Han F, Wang C. Electrochemical Techniques for Intercalation Electrode Materials in Rechargeable Batteries. *Acc Chem Res.* 2017;50(4):1022–31.
25. Pan CJ, Yuan C, Zhu G, Zhang Q, Huang CJ, Lin MC, et al. An operando X-ray diffraction study of chloroaluminate anion-graphite intercalation in aluminum batteries. *Proc Natl Acad Sci U S A.* 2018;115(22):5670–5.
26. Yang C, Chen J, Ji X, Pollard TP, Lü X, Sun CJ, et al. Aqueous Li-ion battery enabled by halogen conversion–intercalation chemistry in graphite. *Nature.* 2019;569(7755):245–50.
27. Li Y, Lu Y, Adelhelm P, Titirici M-M, Hu Y-S. Intercalation chemistry of graphite: alkali metal ions and beyond. *Chem Soc Rev.* 2019;48(17):4655–87.
28. Levi MD, Aurbach D. The mechanism of lithium intercalation in graphite film electrodes in aprotic media. Part 1. High resolution slow scan rate cyclic voltammetric studies and modeling. *J Electroanal Chem.* 1997;421(1–2):79–88.
29. Levi MD, Markevich E, Aurbach D. Comparison between Cottrell diffusion and moving boundary models for determination of the chemical diffusion coefficients in ion-insertion electrodes. *Electrochim Acta.* 2005;51(1):98–110.
30. Yu P, Popov BN, Ritter JA, White RE. Determination of the Lithium Ion Diffusion in Graphite. *J Electrochem Soc.* 1999;146(1):8–14.
31. Yang H, Bang HJ, Prakash J. Evaluation of Electrochemical Interface Area and Lithium Diffusion Coefficient for a Composite Graphite Anode. *J Electrochem Soc.* 2004;151(8):A1247.
32. Piao T, Park SM, Doh CH, Moon SI. Intercalation of Lithium Ions into Graphite Electrodes Studied by AC Impedance Measurements Intercalation of Lithium Ions into Graphite Electrodes Studied by AC Impedance Measurements. *J Electrochem Soc.* 1999;146(8):2794–8.
33. Ong TS, Yang H. Lithium Intercalation into Mechanically Milled Natural Graphite Electrochemical and Kinetic Characterization. 2002;1–8.
34. Chang Y, Sohn H. Electrochemical Impedance Analysis for Lithium Ion Intercalation into Graphitized Carbons Electrochemical Impedance Analysis for Lithium Ion Intercalation into

- Graphitized Carbons. *J Electrochem Soc.* 2000;147(1):50–8.
35. Pfaffmann L, Birkenmaier C, Müller M, Bauer W, Scheiba F, Mitsch T, et al. Investigation of the electrochemically active surface area and lithium diffusion in graphite anodes by a novel OsO₄ staining method. 2016;307:762–71.
 36. Maire P, Kaiser H, Scheifele W, Novák P. Colorimetric determination of lithium-ion mobility in graphite composite electrodes. *J Electroanal Chem.* 2010;644(2):127–31.
 37. Persson K, Hinuma Y, Meng YS, Van Der Ven A, Ceder G. Thermodynamic and kinetic properties of the Li-graphite system from first-principles calculations. *Phys Rev B - Condens Matter Mater Phys.* 2010;82(12):125416.
 38. Verma A, Smith K, Santhanagopalan S, Abraham D, Yao KP, Mukherjee PP. Galvanostatic intermittent titration and performance based analysis of LiNi_{0.5}Co_{0.2}Mn_{0.3}O₂ cathode. *J Electrochem Soc.* 2017;164(13):A3380–92.
 39. Yang S, Wang X, Yang X, Bai Y, Liu Z, Shu H, et al. Determination of the chemical diffusion coefficient of lithium ions in spherical Li[Ni_{0.5}Mn_{0.3}Co_{0.2}]O₂. *Electrochim Acta.* 2012;66:88–93.
 40. Amin R, Chiang YM. Characterization of electronic and ionic transport in Li_{1-x}Ni_{0.33}Mn_{0.33}Co_{0.33}O₂ (NMC333) and Li_{1-x}Ni_{0.50}Mn_{0.20}Co_{0.30}O₂ (NMC523) as a function of Li content. *J Electrochem Soc.* 2016;163(8):A1512–7.
 41. Maire P, Evans A, Kaiser H, Scheifele W, Novák P. Colorimetric Determination of Lithium Content in Electrodes of Lithium- Ion Batteries. *J Electrochem Soc.* 2008;155(11):A862–5.
 42. Yinsheng G, Smith RB, Zhonghua Y, K. ED, Junpu W, Philip K, et al. Li Intercalation into Graphite: Direct Optical Imaging and Cahn–Hilliard Reaction Dynamics. *J Phys Chem Lett.* 2016;7:2151–6.
 43. Fraggadakis D, Nadkarni N, Gao T, Zhou T, Zhang Y, Han Y, et al. A scaling law to determine phase morphologies during ion intercalation. *Energy Environ Sci.* 2020;
 44. Wen CJ, Huggins RA. Thermodynamic and mass transport properties of “LiIn.” *Mater Res Bull.* 1980;15(9):1225–34.

45. Li J, Xiao X, Yang F, Verbrugge MW, Cheng YT. Potentiostatic intermittent titration technique for electrodes governed by diffusion and interfacial reaction. *J Phys Chem C*. 2012;116(1):1472–8.
46. Tsai PC, Wen B, Wolfman M, Choe MJ, Pan MS, Su L, et al. Single-particle measurements of electrochemical kinetics in NMC and NCA cathodes for Li-ion batteries. *Energy Environ Sci*. 2018;11(4):860–71.
47. Ebner M, Marone F, Stampanoni M, Wood V. Visualization and quantification of Electrochemical and Mechanical. *Science (80-)*. 2013;342(November):716–21.
48. Bai P, Cogswell DA, Bazant MZ. Suppression of phase separation in LiFePO₄ nanoparticles during battery discharge. *Nano Lett*. 2011;11(11):4890–6.
49. Meethong N, Huang HYS, Carter WC, Chiang YM. Size-dependent lithium miscibility gap in nanoscale Li_{1-x}FePO₄. *Electrochem Solid-State Lett*. 2007;10(5):134–8.
50. Burch D, Bazant MZ. Size-dependent spinodal and miscibility gaps for intercalation in nanoparticles. *Nano Lett*. 2009;9(11):3795–800.
51. Wagemaker M, Singh DP, Borghols WJH, Lafont U, Haverkate L, Peterson VK, et al. Dynamic solubility limits in nanosized olivine LiFePO₄. *J Am Chem Soc*. 2011;133(26):10222–8.
52. Wei C, Xia S, Huang H, Mao Y, Pianetta P, Liu Y. Mesoscale Battery Science: The Behavior of Electrode Particles Caught on a Multispectral X-ray Camera. *Acc Chem Res*. 2018;51(10):2484–92.
53. Mu L, Yuan Q, Tian C, Wei C, Zhang K, Liu J, et al. Propagation topography of redox phase transformations in heterogeneous layered oxide cathode materials. *Nat Commun*. 2018;9(1):1–8.
54. Finegan DP, Vamvakeros A, Tan C, Heenan TMM, Daemi SR, Seitzman N, et al. Spatial quantification of dynamic inter and intra particle crystallographic heterogeneities within lithium ion electrodes. *Nat Commun*. 2020;11(1):1–11.
55. Flores E, Novák P, Berg EJ. In situ and Operando Raman spectroscopy of layered transition metal oxides for Li-ion battery cathodes. *Front Energy Res*. 2018;6(AUG):1–16.
56. Bai P, Tian G. Statistical kinetics of phase-transforming nanoparticles in LiFePO₄ porous

- electrodes. *Electrochim Acta*. 2013;89:644–51.
57. Zhu Y, Wang C. Novel CV for phase transformation electrodes. *J Phys Chem C*. 2011;115(3):823–32.
 58. Delmas C, Maccario M, Croguennec L, Cras F Le, Weill F. Lithium deintercalation in LiFePO₄ nanoparticles via a domino-cascade model. *Nat Mater*. 2008;7:665–71.
 59. Dreyer W, Jamnik J, Gohlke C, Huth R, Moškon J, Gaberšček M. The thermodynamic origin of hysteresis in insertion batteries. *Nat Mater*. 2010;9(5):448–53.
 60. Sasaki T. Memory effect in a lithium-ion battery. *Nat Mater*. 2013;12(6):569–75.
 61. Kondo H, Sasaki T, Barai P, Srinivasan V. Comprehensive Study of the Polarization Behavior of LiFePO₄ Electrodes Based on a Many-Particle Model. 2018;165(10):A2047.
 62. Bartelt NC, Li Y, Sugar JD, Fenton K, Kilcoyne ALD, Shapiro DA, et al. Simple Stochastic Model of Multiparticle Battery Electrodes Undergoing Phase Transformations. *Phys Rev Appl*. 2018;10(4):044056.

Acknowledgement

P.B. acknowledges the startup support from Washington University in St. Louis. The materials characterization experiments were partially supported by IMSE (Institute of Materials Science and Engineering) and by a grant from InCEES (International Center for Energy, Environment and Sustainability) at Washington University in Saint Louis.

Author contributions

P.B. conceived and supervised the study. S.A. and P.B. designed the experiments. S.A. performed the experiments, carried out the analysis. S.A and P.B. wrote and revised the manuscript.

Additional information

Supplementary information is available online.

Competing interests

The authors declare no competing financial interests.

Data availability

The data that support the findings of this study are available from the corresponding author upon reasonable request.

Code availability

The ImageJ scripts for direct image analysis and MATLAB code for model calculation are available from the corresponding author upon reasonable request.